Numerical and experimental studies of molten pool phenomena influence on dissimilar materials coatings by L-PBF

Amaury Jacquot, Adriana Soveja, Yannick Le Maoult, Christine Boher, Manuel Marcoux, Christophe Escape

Materials Research Proceedings 41 (2024) 12-21 https://doi.org/10.21741/9781644903131-2

Numerical and experimental studies of molten pool phenomena influence on dissimilar materials coatings by L-PBF

JACQUOT Amaury[1,a *], SOVEJA Adriana[2], LEMAOULT Yannick[1], BOHER Christine[1], MARCOUX Manuel[3] and ESCAPE Christophe[4]

[1]Institut Clément Ader (ICA), Campus Jarlard, 81013 Albi, Fance

[2]Institut Clément Ader (ICA), 3 rue Caroline Aigle, 31400 Toulouse, France

[3]Institut de Mécanique des Fluides de Toulouse, Allée Prof. Camille Soula, 31400 Toulouse, France

[4]PROMES -UPR CNRS 8521, France

[a]amaury.jacquot@mines-albi.fr

Keywords: L-PBF Process, Heat Transfer, Multiphysics Model, Characterization

Abstract. Over the past few years, **L**aser **P**owder **B**ed **F**usion (L-PBF) has become increasingly popular, as this method enables energy and material savings during the manufacturing process. 3D L-PBF parts, based on computer-designed geometries, are generated layer by layer using laser energy. Since the beginning of these studies several decades ago, significant progress has been made in the understanding of additive manufacturing, particularly with regard to properties, structure and in situ monitoring. However, the scientific manufacturing community has yet to achieve optimal operational reliability. Presently, numerous defects remain a major problem for parts produced by L-PBF. These defects are mainly caused by the movement of the molten material and its rate of solidification within the melt, which is also influenced by the thermal phenomena of the process. In the L-PBF manufacturing process, the main challenge is to control the complex interdependence of these phenomena [1]. The aim of this work is therefore to study the various physical aspects during a Laser Powder Bed Fusion (L-PBF) process. For this purpose, it is necessary to provide a numerical model with specific works on experimental characterizations of materials at high temperature (up to 1000 °C) as a model's input parameters, such as the thermal or optical properties of cobalt based powder (CoCrMo) used in our study. In addition to material characterization, theoretical model studies have been used to determine the thermal properties of L-PBF powder [2], in particular thermal diffusivity. This model is also validated by specific experimental characterizations, involving the dilution of iron substrates in a CoCrMo alloy deposit and temperature measurements during the manufacturing process. Furthermore, the amount of iron transferred from the substrate to the coating can be used as an indicator of the molten metal movement in the melt and, ultimately, of the operating parameters used to apply the coating. Too much iron on the surface impairs the mechanical strength of the substrate-coating assembly, thus indicates poor control of the parameters used for this purpose [1].

Introduction

Metallic additive manufacturing allows structure fabrication layer-by-layer deposition process and is revolutionizing the manufacturing industry due to its ability to obtain near-net shape products, in a short time span, with almost no material waste. The L-PBF is one of the most used among the additive manufacturing (AM) process [2] and plays an important role in the industry by offering new possibilities of parts shaping, especially for the complex-shape parts. Its principle is to use a heat source to agglomerate a dense material based on pre-deposited layer of powder [3].

However, the AM suffers from certain weakness. Some of AM-made parts have some default like bad homogenization. Depending on the range of the machine parameters like laser scanning

speed, laser power, inner temperature, thermal relaxation time, the shape and the properties of the final part might be different.

To investigate the origins of these issues, we have used the L-PBF process as coating tools. A substrate made of C35 steel has been coated with a thin layer of CoCrMo alloy. In a previous study [4] in the same context, it has been found that iron migration rises into the coating layer. In addition, these dilutions serve as a marker to explain the various physical phenomena present during this AM process and the operating parameters influences on the final results. This work aims to understand the application of L-PBF on these dissimilar materials through an accurate model.

Materials

For both experimentation and numerical modeling, a set of two types of materials have been used: C35 steel alloy as substrates and a CoCrMo alloy, named stellite 21, as coating material. The chemical compositions of both materials are detailed in Tables 1 and 2 respectively.

Table 1 Chemical composition of the C35 steel alloy

Element	Fe	C	Mn	Si	P	S	Cr	Ni	Mo	Cu	Al
Wt%	Base	0.35	0.68	0.21	0.016	0.024	0.19	0.14	0.02	0.17	0.023

Table 2 Chemical composition of the CoCrMo alloy

Element	Co	Cr	Mo	Mn	Fe	Si	P	C
Wt%	63.45	28.9	6.4	0.3	0.2	0.6	0.04	0.11

The particles of CoCrMo alloy powder generally have a spherical shape (Fig.1), with a particle size distribution between 30 and 50 µm.

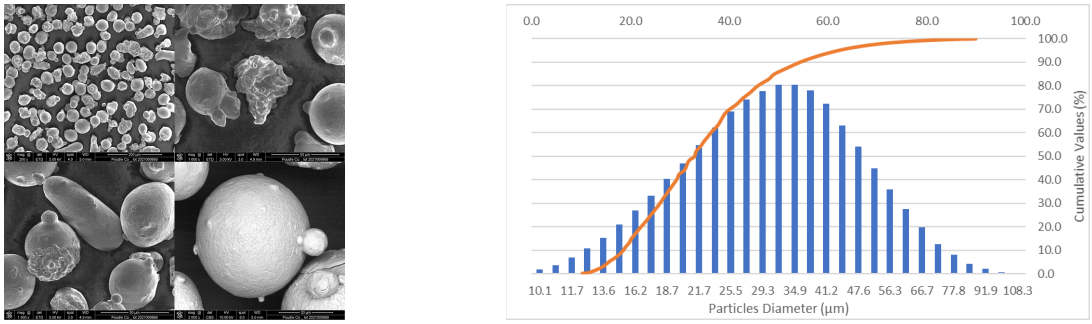

a) b)

Figure 1 SEM observation of the coating powder presenting predominantly a spherical form of particles and some particles having an asteroidal shape (a) and particle size distribution histogram (b)

The properties required to set up the model are well known for the steel composing the substrate. However, little was known about the thermal properties of CoCrMo powder. The next chapter will therefore focus on characterizing these properties.

Diffusivity Measurement

Numerical models have been widely used to understand complex physical phenomena in the printing process, and to study the effect of causal variables on heat transfer, microstructure or residual stresses in printed parts. Heat transfer analysis is a fundamental step in modeling the process. The accuracy of heat transfer analysis relies on accurate characterizations of the material properties, such as density, specific heat, and thermal conductivity. We have carried out the

measurement of thermal diffusivity on this powder, for which there is a lack of data. The thermal diffusivity describes a material's ability to defuse heat through the sample. It is related to transient conduction through the sample and is defined by "α_{th}" as the thermal diffusivity, "k" as thermal conductivity, "ρ" as material density and "C_p" is the heat capacity:

$$\alpha_{th} = \frac{k}{\rho C_p} \quad (1)$$

To evaluate the thermal diffusivity of our powder, we use the Netzsch® LFA 457 micro-flash.This system is composed of a furnace which allows elevating the ambient temperature around the specimen from -125°C to 1100°C. A laser is used to elevate slightly the temperature sample for measurement purpose. To calculate the thermal diffusivity, this system evaluates the time needed for the edge of the sample to reach half the maximum temperature after the pulse heating from the laser. In order to recreate the same measurement conditions as during additive manufacturing, the gas surrounding the sample is argon at atmospheric pressure.

The thermal diffusivity has been measured between the room temperature (30°C) and 1000°C in order to have a good knowledge of this property over the temperature range corresponding to the manufacturing conditions. Three "shots" (punctual measurement) has been made in order to quantify thermal diffusivity uncertainties of these measurements as shown in figure 2 and 3.

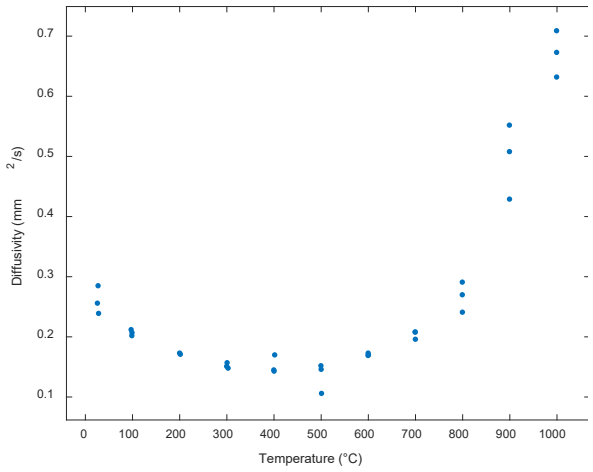

Figure 2 Thermal diffusivity's measurement points

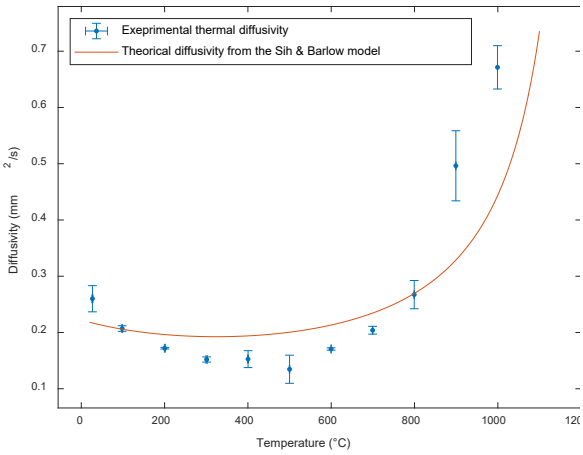

Figure 3 Theoretical and Experimental Thermal Diffusivities

In addition to experimental measurement, some theoretical models have been established to estimate the thermal conductivity, heat capacity and the thermal diffusivity. This article compares thermal diffusivities obtained from theoretical models with those measured. The apparent density was measured and its value is listed in Table 3. As for the heat capacity, a series of measurements was made between room temperature and 300°C [5]. Finally, the thermal conductivity model is based on that of Sih and Barlow. Sih and Barlow model's [6] integrate the Damköhler term (referred to the contribution of thermal radiation) into the Zehner-Schlünder's model to estimate the Equivalent Thermal Conductivity (ETC).

Figure 3 shows a comparison between model-derived and measured diffusivity. Both trends and orders of magnitude agree. However, the experimental thermal diffusivity shows a much more pronounced curvature than the theoretical one. The origin of these discrepancies may lie in the Sih and Barlow model [6], which may neglect some aspects of heat exchange such as the evolution of contact resistance between particles, in particular towards the warmer temperatures. The differences between the two curves may also stem from heat capacity measurements, where we lack certainty as to values and their evolution above 300°C.

Numerical Model

In this work, a two-dimensional heat and mass transfer numerical model is developed to study the CoCrMo-iron interface composition evolution during additive laser manufacturing of the coating. The numerical model is created using a commercial finite element package COMSOL MultiPhysics®. To represent the L-PBF process, we used a 2D model representing the C35 steel cylinder with a thin layer of CoCrMo alloy powder on the top.

Heat dissipation takes place by convection on the vertical and upper walls, and radiation exchanges are only considered on the cylinder's upper edge. The L-PBF support is maintained at 100°C during the coating process. To model the interaction between the substrate and the support, we considered the temperature at the bottom edge at this imposed temperature.

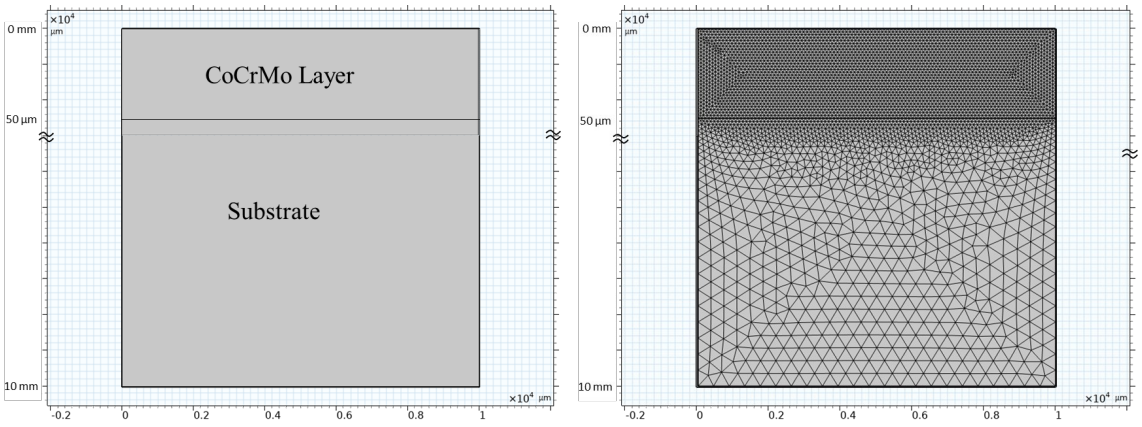

Figure 4 Computation domain and associated mesh

The geometry is meshed with several tetrahedral elements (Fig.4). The mesh generated uses the finest elements in the cobalt powder layer area since this is in this area where the gradient of temperatures and velocities are the most important. With this method, an adaptive mesh, consisting of 15473 tetrahedral elements, has been set up. With the exception of heat capacity and thermal diffusivity, which were measured experimentally for the solid phase.

Heat Transfer Modeling

For the laser heat source model, Gusarov et al [8] proposed to couple the heat transfers and radiation on a homogeneous absorbing scattering medium. Boley et al [9] and Khairallah et al [10], [11] used the ray-tracing method to simulate the input heat flow in a realistic L-PBF process (both on the size of the particles and their array) process. Most generally, authors used a Gaussian shape to model the heat source distribution. Some authors [10] have used a Gaussian surface distribution and others have used a volumetric distribution of the heat source to model the laser-powder interaction. According to Boley et al [9], the laser powder layer interaction takes place mostly one of the first layer of the particle, especially on agglomerates of tiny particles under the laser beam.

In this study the heat source term is used as a volume source with a penetration corresponding to the multi-reflection under the powder layer:

$$Q = \frac{2 \times A \times P_L}{\pi . R_L^2 . \eta} exp\left(\frac{2 \times (x - V_{Laser} \times t)^2}{R_L^2}\right) exp\left(\frac{[z - z_0]}{\eta}\right) \quad (2)$$

Here "A" is the optical absorptivity of the powder, "P_L" is the nominal laser power" R_L" is the projected laser spot, "V_{Laser}" is the scanning speed and "η" being the laser penetration depth. A Gaussian standard deviation corresponding to D4σ method according to Li et al **[12]** with a radius

corresponding to $1/e^2$ of maximal power has been chosen. According to Boley et al **[9]**, it is assumed that the penetration's depth corresponds to the average of the particle size. With a majority of approximately 30µm particle size (Fig.2), it can be supposed that penetration of a non-negligible part of the heat source can be at this depth. With our assumption of that homogeneous medium for the powder, the simplest approach is to consider the particles are disposed on an ideal stacking with one size of particle i.e. the average particle size.

With these assumptions for the heat input, the heat transfers equation for the melted pool can be defined as:

$$\rho C_p \frac{\partial T}{\partial t} - \rho C_p \, \vec{\nabla}(\vec{u}T) + k \, \vec{\nabla}^2 T = q \tag{3}$$

where " ρ " is the density of the material, "C_p" is the heat capacity, "u" is the velocity vector, "k" is the thermal conductivity and " q " is the term combining the various heat sources and losses. Here, we considered the solid part as a liquid with a high viscosity value to neglect any velocity unless the liquidus temperature is reached.

On the edges of the plots, the heat transfers loss is given by:

$$-\vec{n}.\left(-k\vec{\nabla}T\right) = h_\infty(T - T_\infty) + \epsilon\sigma\,(T^4 - T_\infty^4) \tag{4}$$

In this equation, "h" is the convective exchange coefficient, "ϵ" is the thermal emissivity and "sigma" is the Stefan Boltzmann constant. During the melting of the powder layer, the values of ρ, C_p, and k to be used are determined by averaging in powder and liquid phase "f_L". These phases are determined by the condition below:

$$f_L = \begin{cases} 0 & T < T_S \\ \dfrac{T - T_S}{T_L - Ts} & T_S \le T < T_L \\ 1 & T > T_L \end{cases} \tag{5}$$

where "$\boldsymbol{T_S}$" and "$\boldsymbol{T_L}$" are the solidus and liquid temperature respectively. With this condition, an approximative value of the mixture properties like the heat capacity can be calculated:

$$C_p = \frac{1}{\rho}\left\{(1 - f_L)\rho_S C_{pS} + f_L \rho_L C_{pL}\right\} + L_f \frac{\partial \alpha_m}{\partial T} \tag{6}$$

Particularly, only the "C_{pS}" comes from a laboratory in-situ measurement.

For the thermal condition, we calculate its evolution through the temperature between the temperature room (293K) and the Liquidus of each material.

Melt flow Modeling

For the mass flow inside the melt pool, two approaches have been used for the thermomechanical process. For their dissimilar material welding, Métais et al [13] used a RANS k-ω method to represent the multi-vortex phenomena in this context. For the L-PBF model, the main model found is the laminar model [10], [12], [13] with a Newtonian fluid to representing the melted material.

To model the melted metal flow, the conservation of mass is considered:

$$\frac{\partial \rho}{\partial t} + \rho \vec{\nabla}.\vec{u} = 0 \tag{7}$$

and the momentum conservation equation is given as:

$$\rho\left(\frac{\partial\vec{u}}{\partial t}+\vec{u}.\left(\vec{\nabla}.\vec{u}\right)\right)=\vec{\nabla}.\left[-pI+\mu\left(\left(\overrightarrow{\nabla\vec{u}}\right)+\left(\overrightarrow{\nabla\vec{u}}\right)^{T}\right)\right]+F_A+K\vec{u} \quad (8)$$

Here "I" is the diagonal hydrostatic pressure matrix "F_A" is the buoyancy force, "K" is the Darcy damping force and "μ" is the local viscosity. Here we consider the buoyancy forces on the liquid metal induced by the difference of temperature between the center and the edge of the melting pool. With the Boussinesq approximation, we estimate the buoyancy contribution by:

$$F_A = \rho_L\vec{g}\,\beta_T\left(T-T_f\right) \quad (9)$$

where "T_f" is the melting temperature of both Cobalt alloy and steel, "β_T" is the thermal expansion coefficient. The transition from the solid to liquid state is treated with a Darcy condition and the equivalent viscosity methods combined. The first term modifies the viscosity of the medium to give it a deliberately high value, and weakens as soon as the local temperature reaches the melting point. It is applied in this form:

$$\mu = \mu_{solid}+(\mu-\mu_{solid})*flc2hs\left(T,T_{fusion}\right) \quad (10)$$

and the last term is a force to damp the movement outside of the melted area:

$$K=\frac{-C(1-f_l)^2}{f_l^3+b} \quad (11)$$

Where " C " is Darcy's law coefficient deliberately set to a high value to attenuate velocities, "b" is a coefficient to avoid the division by 0 and "f_l"is the local liquid proportion seen in equation (5).

Species transport Modeling

Initial studies of modelling of species transport was carried out for the mixing of species during the welding process of two different materials. These studies were then extended to the context of additive manufacturing [17]. In this work, we consider the movement of the different species inside the melting pool. Being in an area assumed to be liquid, we considered the mix of species by the diluted equation species transports:

$$\frac{\partial\overrightarrow{c_i}}{\partial t}-D_i\vec{\nabla}^2\overrightarrow{c_i}+\vec{u}\times\vec{\nabla}\overrightarrow{c_i}=R_i \quad (12)$$

Where "c" is the local material concentration and "D_i" represent the diffusion coefficient, we considered dependent on the temperature by using the Stokes-Einstein formula

$$D_i=\frac{\kappa\times T}{6.\pi.\mu.r_i}(T>T_m) \quad (13)$$

Simulation Parameters

Finally, the properties of each material are summarized in the table 3 [7]. Note the physicals properties come for the literature excepted the thermal conductivity. For this one, it comes from the characterization of the thermal diffusivity. As explained in the "diffusivity measurement" section, this comes from a calculation based on the definition of this diffusivity and the measurements of each parameter associated with it. In view of the wide temperature variations associated with this type of process, it should be noted that the values are thermally dependent. This is because the behavior of matter is no longer the same between low and "high" temperatures (near melting point).

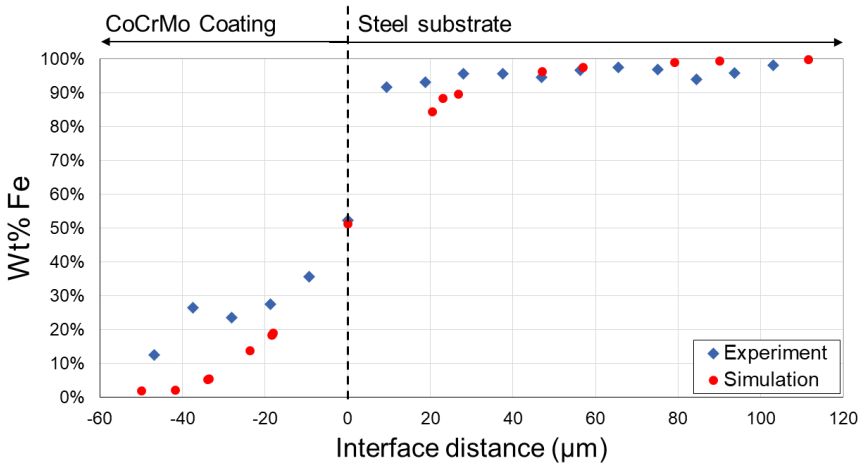

Figure 5 Comparison of experimental and simulated iron dilution near the substrate/coating interface

Results and Discussions

To validate the numerical modeling, the comparison focuses on the proportion of migrated iron near the interface between the substrate and the coating layer with the experimental results, in line with the experimental results obtained by Younsi et al [4]. The dilution is investigated from 110 µm inside the substrate to the upper of cobalt layer (50µm upside) (Figure 5).

This may be due to an underestimation of upward velocities in the molten pool. To find out the reasons for these differences, the heat and mass transfer modes were analyzed from a dimensional point of view.

To take our analysis further, an evaluation of the Reynolds and Rayleigh numbers over time has been made (figure 6), in order to assess their variance before, during and after the passage of the laser source. The Reynolds numbers evaluated show that the material flow is maintained under laminar conditions, validating our basic hypothesis. As for the Rayleigh number, it is used to determine whether buoyancy forces dominate material movement or whether viscous dissipation predominates. The peaks correspond, for both Reynolds and Rayleigh numbers, to instants when the fluidic mechanisms are at their most effective. This makes it possible to evaluate the peak values to check whether the assumptions are valid at all times for Reynolds numbers. But also, to determine the contribution of buoyancy motions before, during and after local melting. These values confirm that buoyancy forces struggle to set the molten metal in motion. Finally, we evaluate the main type of mixing for the present different species occurring in the melt pool. For this purpose, we estimate the ratio between the convective momentum and the diffusion coefficient of the species using the Peclet number. With the obtained result shown by the Fig. 7, the calculated values are well above the critical value of 1, demonstrating that iron migration is mainly due to fluid motion rather than diffusion.

Table 1 : Thermo-physical properties used by the simulation.

Property	CoCrMo	C35 Steel
T Solidus [K]	1598	1609
T Liquidus [K]	1754	1768
T Evaporation [K]	3200	/
Density as solid [kg/m3]	5100	7850
Density as Liquid [kg/m3]	6870	6980
Heat Solid Capacity [J/kg/K]	441.75 + 0.1871×T	604
Heat Liquid Capacity [J/kg/K]	13	758
Thermal conductivity as solid [W/m/K]	Zehner-Schlünder's model **[6]**	51
Thermal conductivity as Liquid [W/m/K]	13	22
Emissivity	0.63	/
Latent heat of fusion [kJ/kg]	310	250
Latent heat of evaporation [kJ/kg]	4961	/
Thermal expansion as solid [1/K]	7.62×10^{-5}	8.5×10^{-5}
Thermal expansion as liquid [1/K]	7.6×10^{-5}	/
Latent Heat Fusion [J/kg]	310×10^{5}	207×10^{5}
Latent Heat Evaporation [J/kg]	4.961×10^{6}	/
Viscosity [Pa*s]	5.5×10^{-3}	5.56×10^{-3}
Marangoni coefficient [N/m/K]	-4.3×10^{-4}	10^{-4}
Absorptivity	0.65	/
Sweep laser velocity [mm/s]	800	
Deposited powder thickness[µm]	50	
Laser power [W]	275	
Laser penetration depth [µm]	30	
Convective horizontal coefficient [W/m/K]	6.5	
Convective vertical coefficient [W/m/K]	9.41	

We can see on this figure that there is a fair agreement correlation between the numerical simulation and the experimental results. However, a difference between the results of around 10% at the substrate-coating interface is highlighted.

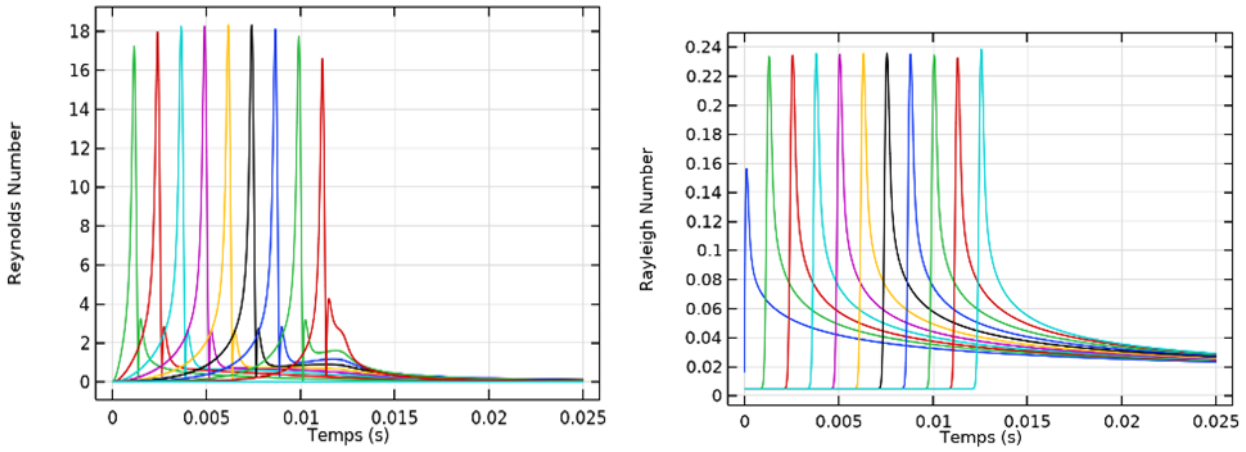

(a) (b)

Figure 6 Evolution of the Reynolds (a) and Rayleigh (b) number through the simulation time.

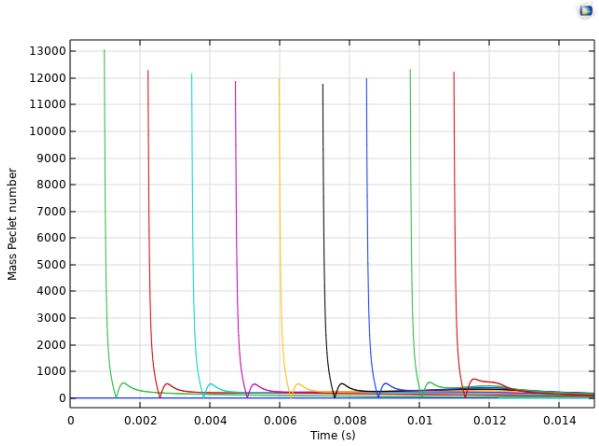

Figure 7 Variations of Peclet (Mass) number inside the melt pool along the simulation time

Based on these results and the correlation between experimentation and simulation results, we can assume that the fluid movements are the main cause of the iron rising inside the cobalt layer. This causes the iron migration from the substrate into the cobalt layer, and the solidification phenomenon has frozen the iron atoms inside the upper layer.

Conclusion

In this article, a model established with characterizations carried out previously has been partially validated by the movement of material from the substrate to the deposited powder layer. However, there is still some fine-tuning to be done to ensure a better agreement between the experimental tests and the numerical modeling.

In order to further improve the present numerical-experimental dilution correlation, the model needs a better following-up of the liquid-solid transition and evaporation mechanism as well. This can be realized by specific numerical methods, starting with followed-up front coupled to Arbitrary Lagrangian-Eulerian (ALE) method. The heat transfer through convection and radiation are, moreover, supposed constant for all times. It is most likely that these transfer modes will change over time.

The final improvement which could be developed in the model is to compare the temperature fields close to the melt to ensure consistency between the model and a L-PBF sweep in a typical manufacturing situation. These temperature measurements will be carried out using non-contact methods, in particular using infrared camera monitoring.

References

[1] C. Boher, T. Younsi, A. Soveja, et M. Chaussumier, « Influence of iron dilution on plastic deformation mechanisms in cobalt-based alloys: Consequence of phase transformations on tribological behavior », *Wear*, vol. 524-525, p. 204845, juill. 2023. https://doi.org/10.1016/j.wear.2023.204845

[2] T. DebRoy *et al.*, « Additive manufacturing of metallic components – Process, structure and properties », *Progress in Materials Science*, vol. 92, p. 112-224, mars 2018. https://doi.org/10.1016/j.pmatsci.2017.10.001

[3] J. P. Oliveira, T. G. Santos, et R. M. Miranda, « Revisiting fundamental welding concepts to improve additive manufacturing: From theory to practice », *Progress in Materials Science*, vol. 107, p. 100590, janv. 2020. https://doi.org/10.1016/j.pmatsci.2019.100590

[4] T. Younsi, C. Boher, et A. Soveja, « Influence of interlayer time on the microstructural state of CoCrMo coatings applied by selective laser melting on an iron-based substrate for different numbers of layers », *Materials Today Communications*, vol. 32, p. 103776, août 2022. https://doi.org/10.1016/j.mtcomm.2022.103776

[5] A. Jacquot, A. Soveja, Y. Le Maoult, C. Boher, et M. Marcoux, « Apport des caractérisations thermiques et thermo-optiques pour le renforcement du lien essais-calculs en fabrication additive L-PBF », 2023. https://doi.org/10.25855/SFT2023-025
[6] S. S. Sih et J. W. Barlow, « The Prediction of the Emissivity and Thermal Conductivity of Powder Beds », *Particulate Science and Technology*, vol. 22, nº 4, p. 427-440, oct. 2004. https://doi.org/10.1080/02726350490501682
[7] W. F. Gale et T. C. Totemeier, Éd., « 8 - Thermochemical data », in *Smithells Metals Reference Book (Eighth Edition)*, Oxford: Butterworth-Heinemann, 2004, p. 8-1. doi: 10.1016/B978-075067509-3/50011-7
[8] A. V. Gusarov, I. Yadroitsev, Ph. Bertrand, et I. Smurov, « Model of Radiation and Heat Transfer in Laser-Powder Interaction Zone at Selective Laser Melting », *Journal of Heat Transfer*, vol. 131, nº 7, p. 072101, juill. 2009. https://doi.org/10.1115/1.3109245
[9] C. D. Boley, S. A. Khairallah, et A. M. Rubenchik, « Calculation of laser absorption by metal powders in additive manufacturing », *Appl. Opt.*, vol. 54, nº 9, p. 2477, mars 2015. https://doi.org/10.1364/AO.54.002477
[10] S. A. Khairallah, A. T. Anderson, A. Rubenchik, et W. E. King, « Laser powder-bed fusion additive manufacturing: Physics of complex melt flow and formation mechanisms of pores, spatter, and denudation zones », *Acta Materialia*, vol. 108, p. 36-45, avr. 2016. https://doi.org/10.1016/j.actamat.2016.02.014
[11] S. A. Khairallah et A. Anderson, « Mesoscopic simulation model of selective laser melting of stainless steel powder », *Journal of Materials Processing Technology*, vol. 214, nº 11, p. 2627-2636, nov. 2014. https://doi.org/10.1016/j.jmatprotec.2014.06.001
[12] Y. Li et D. Gu, « Parametric analysis of thermal behavior during selective laser melting additive manufacturing of aluminum alloy powder », *Mater. Des.*, vol. 63, p. 856-867, nov. 2014. https://doi.org/10.1016/j.matdes.2014.07.006
[13] A. Métais, S. Matteï, I. Tomashchuk, E. Cicala, et S. Gaied, « Dissimilar steels laser welding: Experimental and numerical assessment of weld mixing », *Journal of Laser Applications*, vol. 29, nº 2, p. 022420, juin 2017. https://doi.org/10.2351/1.4983168.
[14] A. K. Mishra et A. Kumar, « Numerical and experimental analysis of the effect of volumetric energy absorption in powder layer on thermal-fluidic transport in selective laser melting of Ti6Al4V », *Optics & Laser Technology*, vol. 111, p. 227-239, avr. 2019. https://doi.org/10.1016/j.optlastec.2018.09.054
[15] M. Bayat, S. Mohanty, et J. H. Hattel, « Multiphysics modelling of lack-of-fusion voids formation and evolution in IN718 made by multi-track/multi-layer L-PBF », *International Journal of Heat and Mass Transfer*, vol. 139, p. 95-114, août 2019. https://doi.org/10.1016/j.ijheatmasstransfer.2019.05.003
[16] Q. Chen, G. Guillemot, C.-A. Gandin, et M. Bellet, « Three-dimensional finite element thermomechanical modeling of additive manufacturing by selective laser melting for ceramic materials », *Additive Manufacturing*, vol. 16, p. 124-137, août 2017. https://doi.org/10.1016/j.addma.2017.02.005
[17] V. Klapczynski *et al.*, « Temperature and time dependence of manganese evaporation in liquid steels. Multiphysics modelling and experimental confrontation », *Scripta Materialia*, vol. 221, p. 114944, déc. 2022. https://doi.org/10.1016/j.scriptamat.2022.114944